Nuclear Engineering and Design 417 (2024) 112811

Contents lists available at ScienceDirect

Nuclear Engineering and Design

journal homepage: www.elsevier.com/locate/nucengdes

Assessing shielding material Performance: Benchmarking of Monte Carlo codes for oil shale and Basalt-Boron fiber concretes

Hando Tohver [a,*], Andrius Slavickas [b], Maryna Holiuk [c], Andrejs Krasņikovs [d], Riho Mõtlep [e], Iveta Nováková [f], Mindaugas Vaišnoras [b], Volodymyr Gulik [a,c]

[a] Institute of Physics, University of Tartu, W. Ostwaldi 1, 50411 Tartu, Estonia
[b] Lithuanian Energy Institute, Breslaujos st. 3, LT-44403 Kaunas, Lithuania
[c] Institute for Safety Problems of Nuclear Power Plants, 12 Lysogirska St, 03028 Kyiv, Ukraine
[d] Department of Theoretical Mechanics and Strength of Material, Riga Technical University, Ķīpsalas iela 6B, LV-1048 Riga, Latvia
[e] Institute of Ecology and Earth Sciences, University of Tartu, Juhan Liivi 2, 50409 Tartu, Estonia
[f] Department of Construction, Energy and Material Technology, The Arctic University of Norway, Lodve Langesgate 2, 8514 Narvik, Norway

A B S T R A C T

Cement-based concretes are commonly used for managing radioactive waste due to their low cost and radiation shielding properties. However, the potential of using oil shale ash as an additive in waste packaging material has been overlooked. This study focuses on benchmarking and developing a Monte Carlo based modeling methodology using multiple transport codes (MCNP, SERPENT, SCALE, OpenMC, and EGSnrc) to assess the effects of these additives on the gamma and neutron shielding properties of concrete. The cross-code comparison showed that all transport codes are in excellent agreement with each other. Investigations into oil shale ash demonstrated similar properties to fly ash. The addition of oil shale ash had a negligible effect on low-level waste (LLW) gamma shielding properties and a minor negative effect on neutron shielding properties. The addition of basalt-boron fibers indicated a minor negative effect on LLW gamma shielding properties but a significant positive effect on neutron shielding properties. The presence of basalt-boron fibers considerably decreased the photon flux resulting from the activation of concrete. In conclusion, this study offers valuable insights into utilizing radiation transport codes to analyze the interactions between radiation particles and innovative concrete additives.

1. Introduction

Cement-based concretes have found wide use in the management of low-, intermediate- and high-level radioactive waste (LLW, ILW and HLW hereafter). Concrete as a waste packaging material is a cost-effective alternative in applications, where the package volume is not a critical design parameter. The high density and quantity of concrete give the packaging excellent radiation shielding properties. Moreover, chemical and physical processes occurring inside concrete immobilize radionuclides present in the waste (Chen et al., 2009; Mallants et al., 2016; Koťátková et al., 2017).

Over the years, many different concrete recipes have been proposed for the purpose of immobilization (Li et al., 2021). Nevertheless, the potential of using oil shale ash (OSA hereafter) in radioactive waste management has been overlooked. OSA is a powdery residue from electric power plants utilizing oil shale. Most of the produced oil shale ash remains unused, being disposed of in local landfills (Loo et al., 2017). This unused and abundantly available substance has demonstrated potentially suitable characteristics as an additive in concrete waste packaging material. OSA has been shown to be rich in hydration products, such as calcium-silicate-hydrate gels, ettringite and monosulfate (Leben et al., 2019), which has demonstrated to have an immobilizing effect on heavy metals (Mallants et al., 2016).

While immobilization of the radionuclides is one of the primary goals of the packaging material, the material must also provide adequate shielding from radiation. For LLW and ILW packaging, the capability to shield gamma-radiation is of key importance. High-density materials and the atomic number of the elements increase the gamma-ray attenuation properties, respectively.

The effect of OSA on gamma-ray shielding properties has not been studied in detail. Still, there have been studies of similar materials, such as fly ash and other industrial residues that can partially replace cement in concrete (Abdullah et al., 2022). Investigations have shown that the addition of fly ash has a negligible effect on the gamma-radiation shielding properties (Singh et al., 2014; Catenacci et al., 2021).

While practically absent in LLW and ILW, the contribution of neutron radiation must be assessed when analyzing potential HLW packaging materials. Similarly to gamma-radiation, blended cement types with fly

* Corresponding author.
E-mail address: hando.tohver@ut.ee (H. Tohver).

https://doi.org/10.1016/j.nucengdes.2023.112811
Received 16 August 2023; Received in revised form 3 November 2023; Accepted 30 November 2023
Available online 12 December 2023

ash have been shown to have comparable neutron shielding properties as Portland cement (Öztürk et al., 2020). To increase the neutron shielding capability of concrete, various neutron moderators and/or absorbers with high neutron capture cross-sections can be added. Concrete already acts as a neutron moderator, mainly through scattering on light hydrogen atoms.

Increasing the neutron shielding capability is most beneficial by introducing other high neutron capture cross-section elements such as gadolinium, cadmium, boron, or cobalt (Piotrowski, 2021). Out of these options, the effect of boron on neutron shielding has been thoroughly demonstrated (Kharita and Yousef, 2011). One potential way to introduce boron into the concrete uniformly is to use boron-infused basalt fibers, which have a remarkably similar specific density to the main components of the concrete (Romanenko et al., 2019).

The evaluation of shielding properties can be a complicated endeavor. While gamma and neutron shielding properties can be experimentally measured, this requires working with radiation sources in close proximity, which can be expensive and yield less information about the samples than alternative modeling approaches. Additionally, the difficulty in constructing innovative waste packages can be prohibitively expensive. The most flexible shielding evaluation techniques are based on the Monte Carlo method. Monte Carlo radiation transport codes do not set general requirements on the modeled scenario or materials, while providing plentiful information through the use of various tallies.

A Monte Carlo study investigating basalt-boron fiber (BBF hereafter) concrete in the reactor environment demonstrated the positive effects such additives can have on thermal and fast neutron shielding properties (Zorla et al., 2017). However, most previously done studies have relied on a single particle transport code and only used total volume averaged flux to describe the effect of boron in concrete.

Most Monte Carlo codes are well-validated and thoroughly tested, but largely export-restricted, limiting the availability of a model-based shielding evaluation approach significantly. There are open-source options, but these are often relatively new, more complicated to use, or not as popular. In order to characterize innovative concretes and make the methodology more accessible, a benchmarking study using realistic concrete descriptions and various codes is necessary.

To investigate the effects of OSA and BBF as potential waste packaging concrete additives, this study will first use multiple well-validated transport codes such as MCNP, SERPENT, SCALE, OpenMC, and EGSnrc to investigate and cross-compare potential gamma and neutron particle flux energy spectra for realistic radioactive waste sources. By relying on multiple code evaluations, the interactions between concrete with innovative additives and radiation particles can be described with great accuracy and detail. These investigations are supplemented by neutron activation calculations and subsequent activation photon spectra analysis.

2. Methodology

To model and assess the radiation shielding capability of concrete enhanced by OSA and BBF, the chemical composition of the concrete must be determined. For this purpose, multiple concrete recipes were created and each of the ingredients was measured using XRF spectroscopy. Based on the ingredient characterization and concrete recipes, the radiation shielding capability of the concretes was assessed by simulating the composite materials using Monte Carlo particle transport codes.

2.1. Material description

The material investigations were done in two parts. First, a cross-comparison of radiation transport codes was done by modeling an industry standard Portland concrete characterized by NIST (Berger et al., 2017). Secondly, the effect of OSA in concrete was analyzed by creating 25 unique concrete mixes with varying OSA concentrations, oil shale ash source, and water content. All of the concrete tpyes contained basalt fibers.

Table 1
The concrete recipes of 4 concrete mixes experimentally created during this study.

Ingredients / Recipes	XH concrete	OL-A concrete	OH-E concrete	OL-E concrete
Schwenk Eco cement CEM II A-LL 42.5 N	9.52 %	8.69 %	7.40 %	8.68 %
OSA	0 %	4.67 %	3.99 %	4.66 %
Water	8.21 %	7.65 %	9.82 %	7.45 %
Dolomite 4–8 mm	26.26 %	31.40 %	2.36 %	31.35 %
Sand 0.3–2.5 mm	26.59 %	31.79 %	41.23 %	31.74 %
Sand 0–1.0 mm	20.68 %	8.63 %	24.74 %	8.62 %
Dolomite flour	7.88 %	5.69 %	9.42 %	5.68 %
Plasticizer	0.30 %	0.59 %	0.35 %	0.59 %
Microsilica	0 %	0.20 %	0 %	0.20 %
DBF fibers 24 mm	0.58 %	0.69 %	0.69 %	1.03 %

The quantities are given in kilograms (weight fraction percentages). The table is missing XH-B concrete, which was a modified version of the XH concrete (modeled).

Concrete samples were fabricated using OSA from two different geographical places in Estonia. The main ingredients in the concrete were: Sand 0–1.0 mm, Sand 0.3–2.5 mm, Dolomite flour, Dolomite gravels 4–8 mm, Schwenk Eco cement CEM II A-LL 42.5 N, Oil shale ash (OSA), Water, Plasticizer (Sika D190) and Basalt fibers (DBF Turbobuild integral 24 mm long). First, the dry materials were mixed - cement, OSA, fine aggregates and coarse aggregates.

After 3–4 min of mixing, 60 % of the total amount water and plasticizer was added. During the next 5–6 min of stirring, the remaining water was added. After the consistency control (stirring was continued with the goal to avoid concrete lumps formation) fibers were added into the mix in small portions. Main reason for adding the fibers at the end was to protect “fibers agglomerates” and “balls” formation in the concrete mix. Fiber concrete rheological properties were evaluated using the Abrams cone settlement. Finally, each fresh concrete mix was mixed for another 2–3 min and then filled into cube and prism molds. After 2–3 days, samples were removed from the molds and placed in a water bath with a constant temperature of water 20 ± 2C. After 28 days, the samples were subjected to chemical analysis. Out of the 25 experimentally created concrete mixes, four final recipes (Table 1) were modeled using the transport codes. One additional concrete mix was modeled by determining the concrete with best neutron-shielding properties and then modifying the chemical composition of that concrete by replacing 100 % of basalt fibers with BBF.

Together with the modeled BBF concrete, the properties of five different concrete types were compared to each other. Three concretes had a water content of 8–10 % (in respect to the total mass of all the ingredients), while two concretes had a lower water content close to 7.5 %. These concrete types were labeled respectively for low (L) or high (H) water content. One concrete was used as a baseline and did not include any OSA (labeled with an X). The same concrete was used to model BBF as well (label B). In the other three concretes, 35 % of the cement was replaced with OSA (label O). Depending on the source of OSA, the concretes were labeled after either Auvere oil shale power plant (A) or Eesti Energia Power Plant (E). The chemical composition and density of the concretes are described in Table 2.

While gamma shielding properties can be effectively modeled based on simple elemental composition, neutron shielding is heavily dependent on the isotopic distribution of each element present in the material. Since isotopic composition could not be characterized with the available laboratory equipment, each element was divided into its known naturally occurring isotopic composition (Meija et al., 2016).

One stark difference between NIST concrete and other recipes evaluated in this study is the hydrogen content. NIST concrete has roughly

Table 2
Densities (g/cm^3) and elemental weight fractions of modeled materials.

	NIST air, dry	NIST concrete	XH concrete	XH-B concrete	OL-A concrete	OH-E concrete	OL-E concrete
ρ	1.205E-03	2.300	2.301	2.301	2.333	2.251	2.339
H		2.210E-02	1.138E-02	1.138E-02	9.222E-03	1.138E-02	8.989E-03
B				1.325E-04			
C	1.240E-04	2.484E-03					
N	7.553E-01						
O	2.318E-01	5.749E-01	5.044E-01	5.045E-01	4.551E-01	5.092E-01	4.542E-01
Na		1.521E-02	3.983E-03	3.856E-03	3.348E-03	4.137E-03	3.453E-03
Mg		1.266E-03	3.144E-02	3.149E-02	8.633E-02	3.181E-02	8.630E-02
Al		1.995E-02	1.794E-02	1.788E-02	1.608E-02	1.783E-02	1.634E-02
Si		3.046E-01	2.761E-01	2.761E-01	1.867E-01	2.855E-01	1.873E-01
P			2.002E-04	1.771E-04	1.733E-04	1.892E-04	1.865E-04
S			1.127E-03	1.126E-03	1.058E-03	9.473E-04	1.057E-03
Cl			9.881E-06	9.908E-06	2.060E-05	1.922E-05	2.092E-05
Ar	1.283E-02						
K		1.005E-02	1.032E-02	1.030E-02	8.920E-03	1.045E-02	8.956E-03
Ca		4.295E-02	1.307E-01	1.307E-01	2.200E-01	1.176E-01	2.199E-01
Ti			5.820E-04	5.187E-04	6.231E-04	5.443E-04	6.772E-04
V				3.035E-06			
Cr			1.674E-05	1.674E-05	1.756E-05	1.535E-05	1.753E-05
Mn			4.522E-04	3.538E-04	7.488E-04	4.377E-04	8.011E-04
Fe		6.435E-03	1.089E-02	1.091E-02	1.116E-02	9.517E-03	1.139E-02
Co			3.828E-05	3.844E-05	2.159E-05	3.702E-05	2.155E-05
Ni				1.032E-07	7.546E-07	6.440E-07	7.534E-07
Cu			5.881E-06	6.047E-06	4.519E-06	3.823E-06	4.512E-06
Zn			2.741E-05	2.816E-05	2.078E-05	2.044E-05	2.075E-05
Ga			3.283E-06	3.386E-06	2.430E-06	2.989E-06	2.426E-06
Ge			6.838E-06	6.838E-06	2.414E-06	6.838E-06	2.410E-06
As					4.660E-08		4.653E-08
Se					3.689E-08		3.683E-08
Br			2.881E-06	2.881E-06	1.208E-05	2.713E-06	1.206E-05
Rb			2.740E-05	2.782E-05	2.450E-05	2.622E-05	2.446E-05
Sr			1.394E-04	1.414E-04	1.687E-04	1.205E-04	1.685E-04
Y			8.402E-07	1.161E-06	6.413E-07	5.461E-07	6.404E-07
Zr			2.066E-05	2.083E-05	1.242E-05	2.066E-05	1.240E-05
Nb			6.001E-07	6.001E-07	4.581E-07	3.901E-07	4.574E-07
Mo			5.281E-06	5.281E-06	4.031E-06	3.433E-06	4.025E-06
Ba			1.413E-04	1.430E-04	1.030E-04	1.360E-04	1.029E-04
Sm			6.877E-05	6.877E-05	5.250E-05	4.470E-05	5.242E-05
Pb			1.138E-05	1.161E-05	8.744E-06	8.821E-06	8.731E-06

double the hydrogen concentration as other concretes considered in our research. The chemical composition of oil shale concrete ingredients was determined using the XRF method, which did not enable the determination of hydrogen content. Since added water was the only hydrogen source, the described concretes would have an underestimated hydrogen content compared to the NIST concrete.

The difference in hydrogen levels would lead to a biased comparison due to hydrogen's well-known ability to moderate neutrons. Therefore, only the comparison between different OSA and BBF concretes was presented in the results sections as these chemical compositions were determined using the same methodology. Comparison of these concretes to other well-studied recipes will be done in a future paper, where the composition of light elements will be studied and presented in more detail.

Another subtle difference in the recipe of the above-presented concretes is basalt fiber content. XH, OL-A, and OH-E concrete types included 0.7 % of basalt fibers by weight, while the content of OL-E concrete had a higher content of 1 %.

Since basalt fiber is a product derived from basalt stone, it has considerable durability. Therefore, its outstanding characteristics are particularly valuable in the nuclear energy industry, where the requirements for the long-term durability of structures are very stringent due to their significant service life (about 100 years for nuclear reactors (including construction time, operation time, decommissioning time) and at least several hundred years for radioactive waste storages and spent nuclear fuel storages) (Ageing management of concrete structures in Nuclear Power Plants, 2016). BBF is a modified basalt fiber with boron oxide added during manufacturing. In this way, boron in concrete

Table 3
General transport settings for compared radiation transport codes.

	MCNP	Serpent	OpenMC	SCALE	EGSnrc
Photon min. threshold	10 keV				
Photon max. threshold	100 GeV	100 MeV	50 MeV	20 MeV	50 MeV
Neutron min. threshold	10^{-5} eV	10^{-5} eV	10^{-5} eV	10^{-5} eV	–
Neutron max. threshold	20 MeV	20 MeV	20 MeV	20 MeV	–
Photon cross-sections	ENDF.VII.1				EPDL97
Temperature (cross-section data)	300 K	300 K	293 K	293 K	–
Neutron cross-sections	ENDF.VII.1				–
Temperature (cross-section data)	293 K	294 K (H-1, & H-2)	293.6 K (H-1, & H-2)	293 K293.6 K (H-1 & H-2)	
Thermal scattering	H in H_20				–
Batches	10				
Particles per batch	10 000 000				

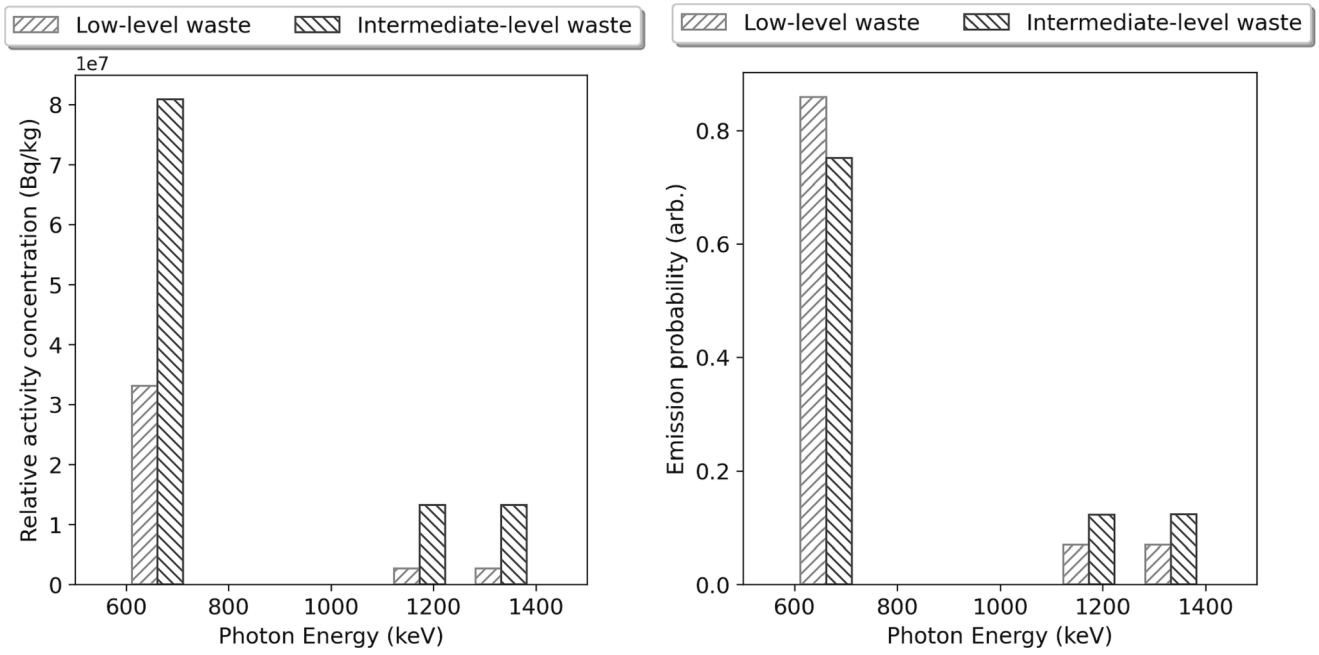

Fig. 1. LLW and ILW gamma-ray spectra of Ignalina NNP waste inventories.

is present inside the basalt fiber matrix, which ensures that boron does not have a negative effect when it is directly added to concrete (Zorla et al., 2017). With this BBF addition to the concrete, some of the mechanical characteristics of the concrete are also improved. In this paper, BBF contains 6 % boron oxide (B_2O_3), although experimental studies have shown that up to 12 % boron oxide can be added to basalt fiber without degrading the mechanical characteristics of the fiber.

2.2. Radiation transport codes

To achieve high confidence in the modeling results, a cross-code comparison between MCNP, Serpent, OpenMC, SCALE and EGSnrc was conducted. Moreover, any key differences between these codes can be illustrated and analyzed by comparing the model outputs.

First, all codes must use comparable nuclear cross-section libraries. For this purpose, ENDF/B.VII.1 was selected as all codes either supported the use of this library or used analogous data. A summary of the transport settings for each code is presented in Table 3 and a short description of the code is provided below. It should be noted that no variance reduction methods were applied for any of the codes.

2.2.1. Mcnp

MCNP is a general-purpose Monte Carlo code for transporting neutrons, photons, electrons, and other charged particles over a wide range of energies. As with most Monte Carlo codes, MCNP allows for creating complex 3-D model geometries, specifying different particle sources, and acquiring input information using different detectors. In this work, the MCNP6.2 version is used (Werner, 2017).

2.2.2. Serpent

Serpent is a multi-purpose three-dimensional continuous-energy neutron and photon transport code developed at VTT Technical Research Center of Finland (Leppänen et al., 2013). Initially, the code was developed for spatial homogenization problems in reactor calculations, but over the years of development, it has acquired many additional capabilities that go beyond neutron calculations of nuclear facilities. Among these implementations are the development of an advanced automated CAD design function and the introduction of unstructured geometry based on several types of geometric meshes. Serpent can facilitate the simultaneous transport of neutrons and photons. Serpent version 2.1.31 was used for the simulations in this paper.

2.2.3. Scale

The SCALE code system provides a comprehensive toolset for criticality safety, reactor physics, radiation shielding, radioactive source term characterization, sensitivity, and uncertainty analysis (Wieselquist et al., 2020). Monaco is a 3-D Monte Carlo code developed within SCALE to calculate neutron and photon fluxes and responses to specific geometry regions, point detectors and mesh tallies. The second-order surface SCALE general geometry package (SGGP) is used for the geometry construction within Monaco. Monaco uses the same cross-section data package as other SCALE modules. All cross-section libraries available within SCALE 6.2.4 were processed from ENDF/B-VII.0 or -VII.1 evaluated data files using the AMPX code system (Wiarda et al., 2016). These processed libraries include 19 thermal-scattering moderators for which bound-scattering kernels are provided in ENDF/B-VII.0 and ENDF/B-VII.1.

2.2.4. Egsnrc

EGSnrc is an open-source 3-D Monte Carlo radiation transport code used to simulate photons, electrons, and positrons with energies from 1 keV to several tens of GeV. Similarly to MCNP, EGSnrc has photon and electron transport coupled together. EGSnrc can simulate any photon-electron interactions in a high level of detail (with a focus on low-energy interactions), but at the same time making it more complicated to conduct a one-to-one comparison with pure neutronics codes with added support for photons. For this study, the simulations were configured using standard EGSnrc (2021) settings with the EPDL97 cross-section library. Since other neutronics codes used ENDF/B data libraries, EPDL97 was chosen for better comparison as the ENDF-VII.1 uses EPDL97's photon interaction data (Han et al., 2018). Finally, a pre-written *egs-kerma* library was used to score volume averaged flux in target regions.

2.2.5. OpenMC

OpenMC is an open-source Monte-Carlo 3-D neutronics code with added support for photon transport (Romano et al., 2015). The geometry was defined using the built-in constructive solid geometry (CSG) method

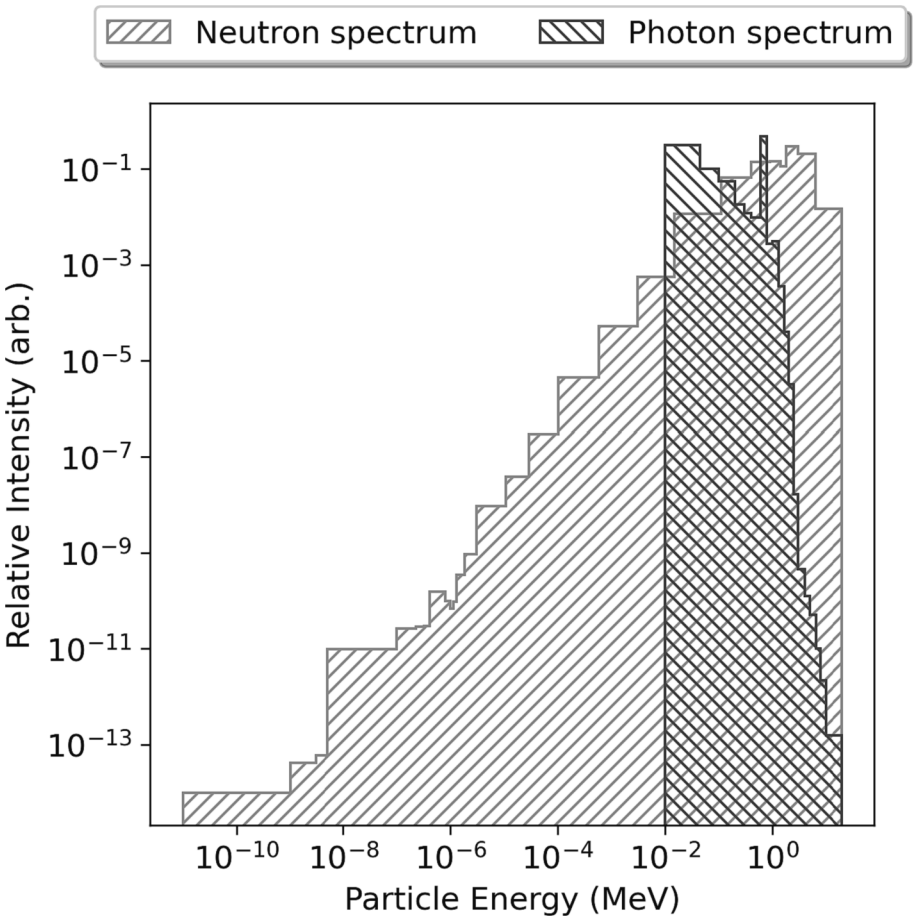

Fig. 2. Spent nuclear fuel photon and neutron emission spectra.

through the Python API. Similarly to EGSnrc, the configuration was kept standard (v0.13.2), using the thick-target bremsstrahlung (TTB) approximation. ENDF/B-VII0.1 was used with thermal scattering data for hydrogen in water.

2.3. Radiation source description

2.3.1. Low-Level waste

To evaluate the shielding capability of concrete for realistic radiation energies, the emission spectra of Ignalina's LLW and ILW were investigated. Based on the radionuclide composition of the waste, gamma-photon emission spectra could be created. This was done by converting the relative activities of various radionuclides into gamma-emission lines. The gamma-emission data was sourced from the LNHB's gamma-emission libraries (Bé et al., 2013). Since the original age of the waste was known, the progeny emissions could be retroactively taken into account by using a Python script, which incorporated the "radioactivedecay" module for the activity decay calculations. The modules enabled the incorporation of decay chains into the creation of the emission spectrum.

While the script-based approach made the generation of the spectrum mostly automated, the individual emission lines of radionuclides were independently verified to catch any double counting of emission lines. This double counting was observed for several decays, where the description of *meta*-stable isotopes did not match between the "radioactivedecay" Python module and LNHB's gamma-emission data. Any such discrepancies were corrected by matching the *meta*-stable isotope description of the LNHB files with the Python module. The generated spectra are described in Fig. 1.

More than 99.5 % of the emission probability was contributed by just two radionuclides – Co-60 and Cs-137. The main emission lines for these radionuclides are visible on the emission spectra. By far, the greatest contribution is from the 661 keV line emitted by Cs-137, making up 85 % of the emissions for the LLW and 75 % for ILW. The third highest emission intensity came from the decay of Nb-94. However, the emission intensities were several orders of magnitude smaller than Co-60 and Cs-137. The Co-60 and Cs-137 sources were chosen for the radiation shielding analysis and modeled as a continuous-energy discrete spectrum.

2.3.2. Spent nuclear fuel

Irradiation of LLW packaging can be characterized by the modeling of gamma-photons. If similar materials were used for spent nuclear fuel (SNF hereafter), they need to demonstrate an adequate shielding capability of neutrons. Similarly to LLW, the SNF description was taken from the fuel generated at the Ignalina site. Due to the abundance of radionuclides in spent fuel, the packaged material was not described through the activity of constituent radionuclides, but through gamma-photon and neutron emission spectra. These spectra are visualized in Fig. 2 below.

The gamma-photon and neutron emission spectra were evaluated using the SCALE code. RBMK-1500 fuel assembly loaded with 2 % U-235 enrichment fuel was depleted using the TRITON/TEWT sequence assuming mirror boundary conditions and typical operational parameters for Ignalina NPP till it reached 13.75 GWd/tU burnup. ORIGEN module was used to estimate gamma-photon and neutron emission spectra after 7958 days (about 22 years) of cooldown.

The SNF's emission spectrum of photons ranged from 10 keV to 2 MeV. The neutron emission spectrum ranged from thermal to fast neutrons. Both spectra displayed the highest emission intensities near the

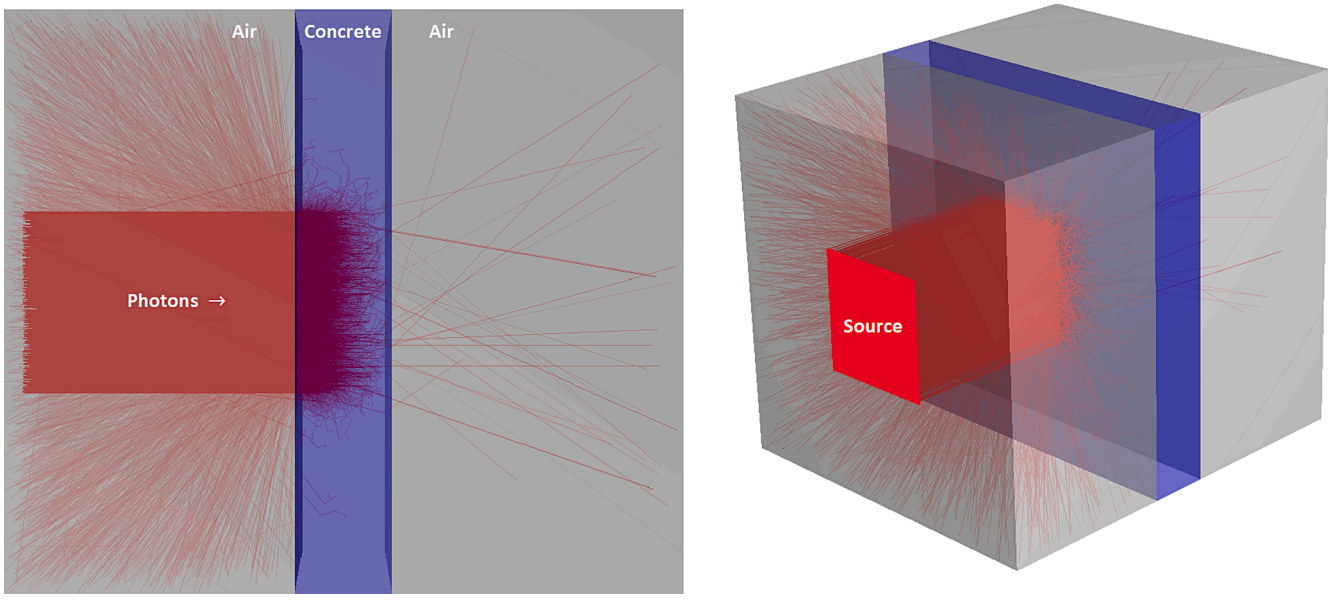

Fig. 3. Geometry of the model visualized in EGSVIEW with photon (red) tracks. Air is colored gray and concrete blue. Isometric view of the model geometry is given on the right while side-view is provided on the left.

MeV energy range. However, while the intensity of neutron emissions increased with energy, the photon intensities decreased, except for a local peak near 1 MeV. The emission spectra on neutrons were modeled as histogram sources.

2.4. Model geometry and scoring

The modeled LLW and SNF emissions were incorporated into the simulation universe as a collimated 150 cm x 150 cm plane source. The source was directly aimed at the rectangular block of concrete. Between the source and concrete was 150 cm of air. The concrete itself was modeled as 5 layers, each having a depth of 10 cm, a width and a height of 350 cm. The concrete was followed by two layers of air. The initial 10 cm of air right behind the concrete was used for scoring and after that followed 140 cm of additional buffer air. The model is visualized in Fig. 3. The simplified model was used to investigate the material properties while making it possible to study how the materials modify the gamma-photon and neuron energy flux spectra in the material and close proximity to it. As an added bonus, the simplified model description made it easier to conduct the cross-comparison of codes presented in the study.

Each particle transport code used the same geometry and tallied the total volume averaged flux and volume averaged flux energy distribution. The tallies were constructed for all 5 concrete layers and for the initial 10 cm air layer behind the concrete. On average, 50 cm of concrete was enough to attenuate 99.9 % of the radiation directed at the concrete.

Evaluating the accuracy of the models can be a difficult challenge as there is no known correct value for this model calculation. One way to evaluate the relative accuracy is to compare the different transport code outputs to each other. The comparison of transport code outputs was implemented through an arithmetic mean of all the numerical values corresponding to individual volume layers and energy bins. The relative error (*RE*) of each code from the average of all codes was calculated

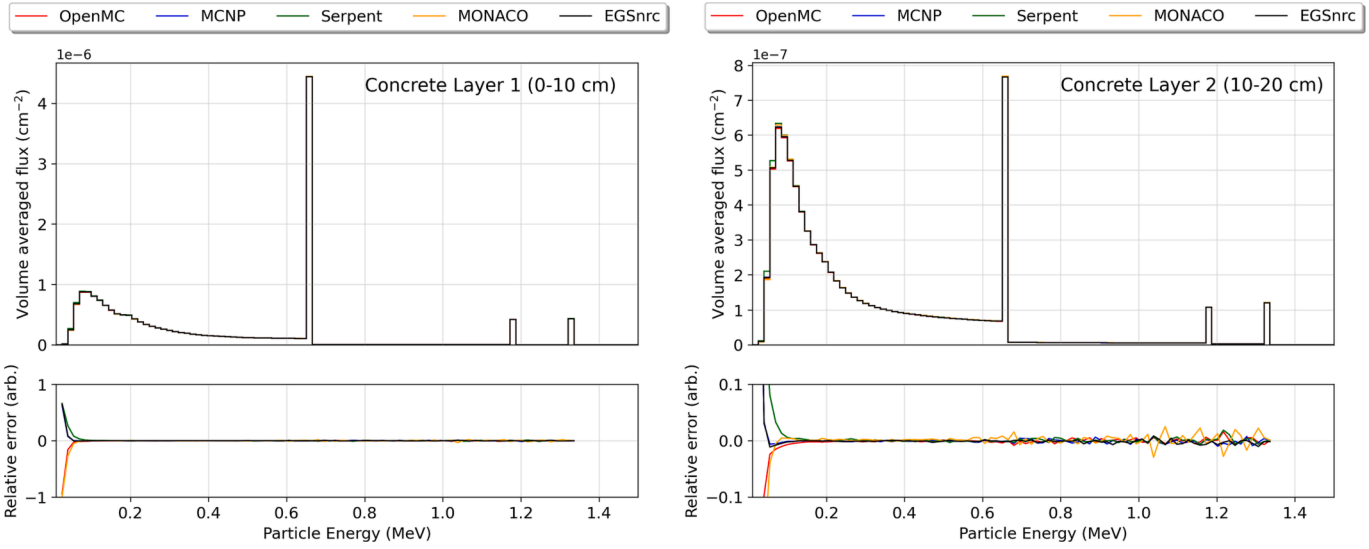

Fig. 4. Volume averaged flux in concrete layers 1 and 2 in relation to particle energy. The upper plots show the volume averaged photon flux spectra from various codes while the lower plots describe the relative error from the mean of all codes.

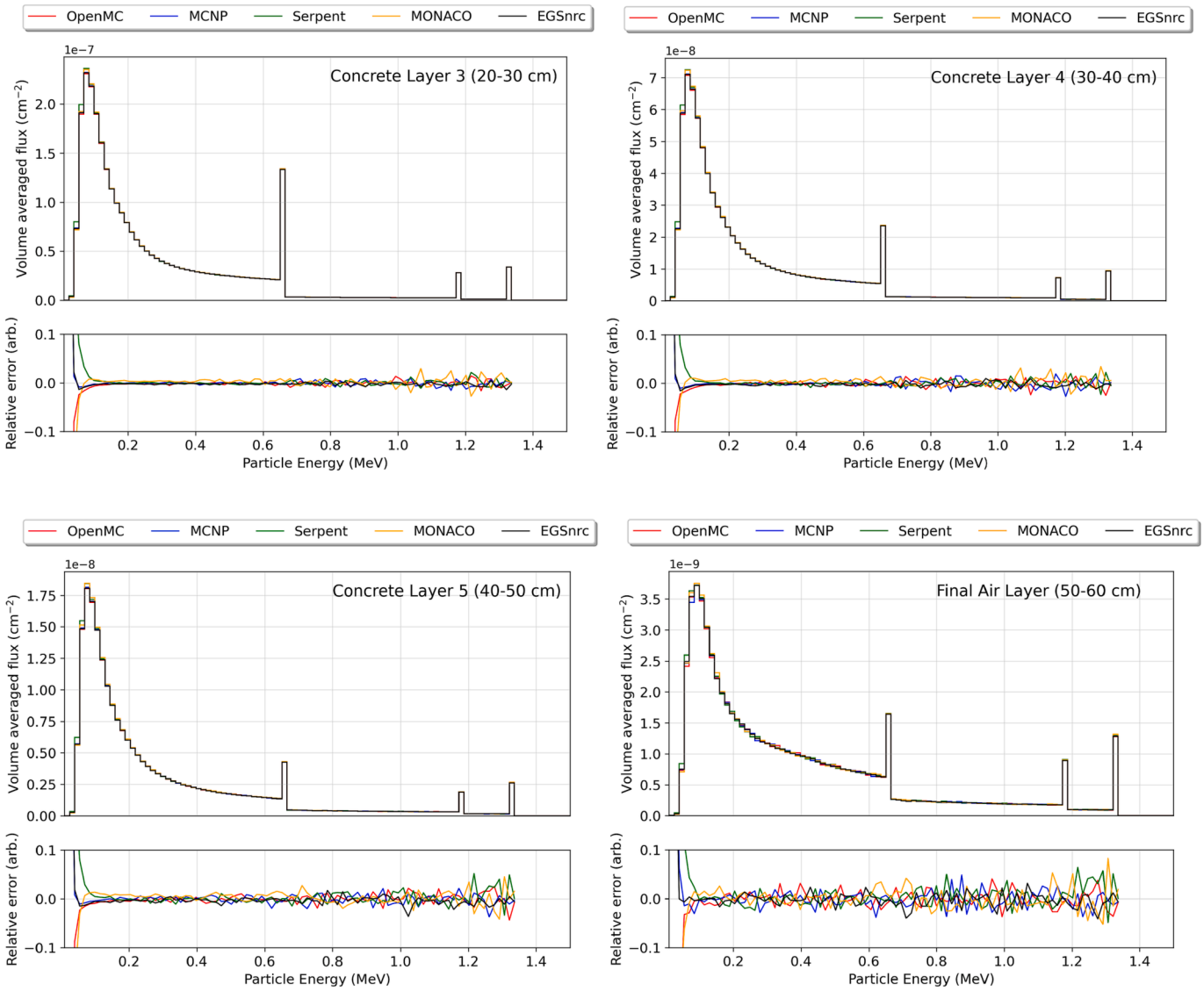

Fig. 5. Volume averaged flux in concrete layers 3–5 and air in relation to particle energy. The upper plots show the volume averaged photon flux spectra from various codes while the lower plots describe the relative error from the mean of all codes.

using the following formula:

$$RE = \frac{Output_{code}}{Output_{average}} - 1$$

If the code and average output have a total agreement, the relative error would be 0.

All Monte Carlo simulations are also accompanied by statistical errors, which are fundamentally attributable to the nature of the method. These errors can be minimized by simulating more particles or batches, but never eliminated altogether. For this study, 10^8 particles were simulated for each source type to characterize the total flux per tallied volume as well as the flux's energy distribution. The particle energy was measured using 100 bins. The LLW source calculations used linearly scaled energy bins, while the SNF source flux tally was divided using a logarithmic scale.

3. Results and discussion

3.1. Validation of photon flux in standard concrete from LLW source

The management of LLW and ILW requires materials with excellent gamma-photon attenuation properties. Using the LLW source term described in the methods, the volume averaged flux was tallied for each of the 5 concrete layers. The immediate air layer after the concrete was investigated as well. The simulation results for all five particle transport codes (volumetric flux energy distribution) are reported in Figs. 4 and 5. The LLW photon flux simulations had statistical errors no higher than 5 % for most energy bins. Only for the first four energy bins (10 keV to 70 keV) was the error significantly higher (between 5 % and 30 %). For the flux values in concrete, average statistical errors remained below 1 %.

The approximate shape of the energy distribution remains fixed in all the tallied layers. Four peaks can be singled out from the spectra. The initial wide low-energy peak is mostly due to the Compton-scattering taking place within the material, but to some extent attributable to the bremsstrahlung as well. The following high energy peak around 660 keV is the characteristic emission line for Cs-137. Finally, Co-60 is responsible for the 1170 keV and 1330 keV peaks.

The codes show excellent agreement for most of the energy bins. The relative error from the arithmetic means for layers 1 and 2 is on average less than 0.05. Larger errors do appear for the few energy bins below 100 keV. In part, these errors are from the low tally count for low-energy bins, which increases the statistical error and difference between codes.

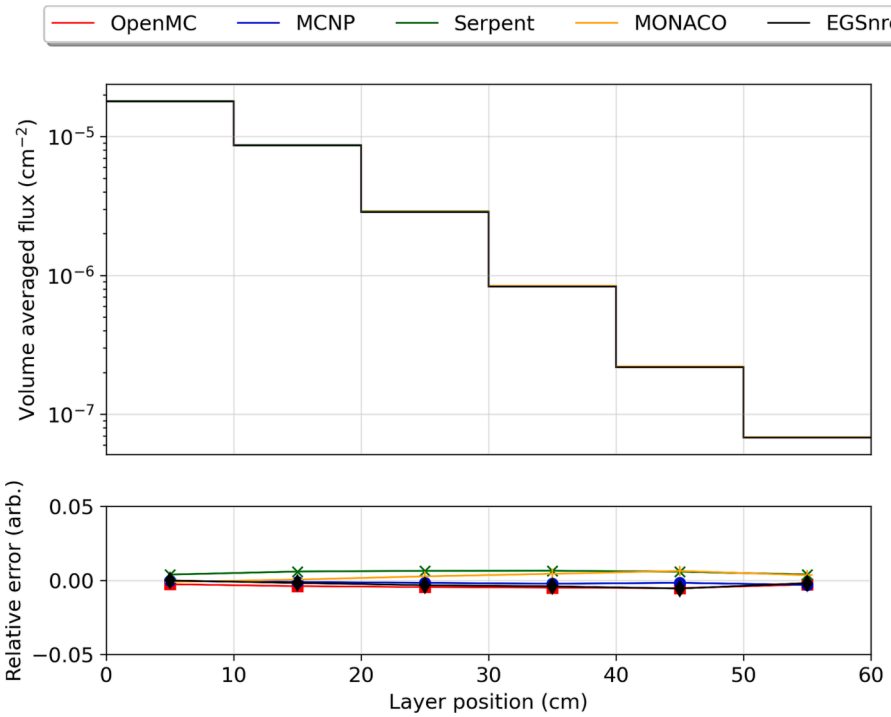

Fig. 6. The upper plot displays the comparison of volume averaged photon flux spectra from various codes. Flux is presented in relation to tallied layer positions. The lower plot describes the relative error (deviation from the mean of all results).

While the errors are high, the volumetric fluxes for these bins are insignificant compared to the high-intensity peaks mentioned above. For this reason, the relative error (except the first layer), is shown in higher detail to demonstrate the values for the majority of the energy bins. With the following layers, the relative intensities of peaks change (Fig. 5).

The increase in the intensity of the Compton scattering peaks can be explained by the built-up equilibrium conditions inside the concrete. As the emitted gamma-rays undergo interactions, part of their energy is deposited. The resulting lower-energy particles keep travelling through the concrete, moving from one layer to another. Layers in the middle can reach quasi-equilibrium conditions, where the in-scattering of Compton photons can be approximately equal to the out-scattering of photons from a region. While the true equilibrium cannot be reached as the flux of particles is decreased in each subsequent volume, the shape of the energy distribution remains roughly constant.

The relative error in the following layers shows small increases in the deviation, which can be partly attributed to the decrease in flux (order of magnitude decrease in flux for each passing layer). There are no discernible biases in the code outputs, which show good agreement. The results indicate that after configuring the codes to have minimal differences in cross-sections and transport settings, any difference in transport algorithms has minimal effect on the final volumetric flux in the 100 keV – 1330 keV energy region. This is further confirmed by looking at the total volume averaged flux in all tallied layers, as shown in

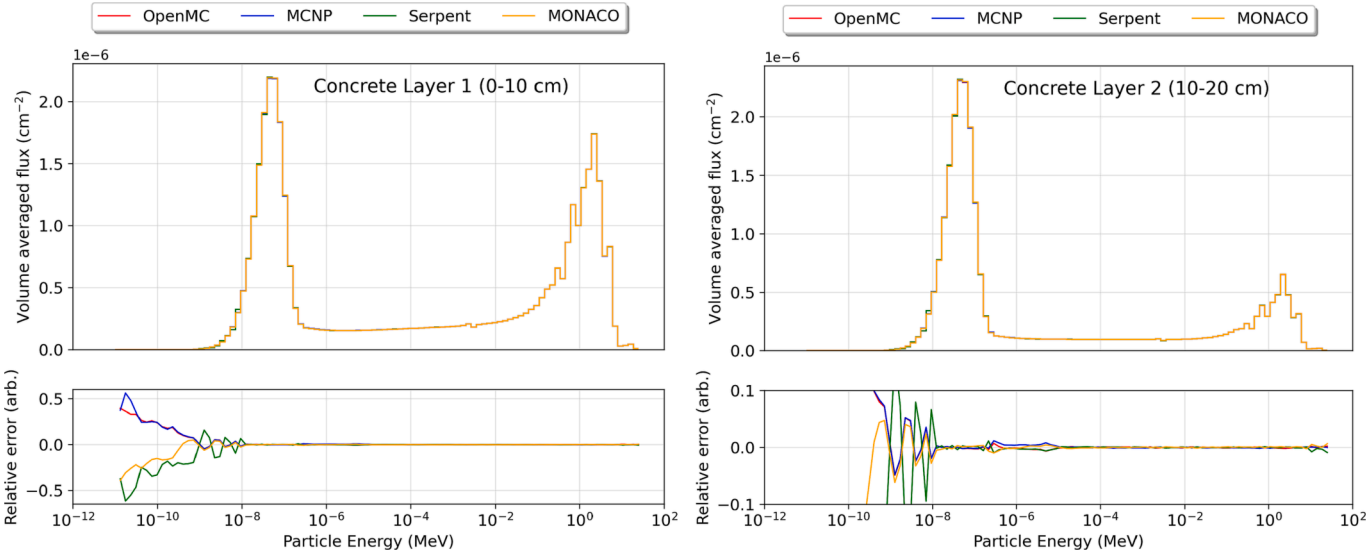

Fig. 7. Volume averaged flux in concrete layers 1 and 2 in relation to particle energy. The upper plots show the volume averaged neutron flux spectra from various codes while the lower plots describe the relative error from the mean of all codes.

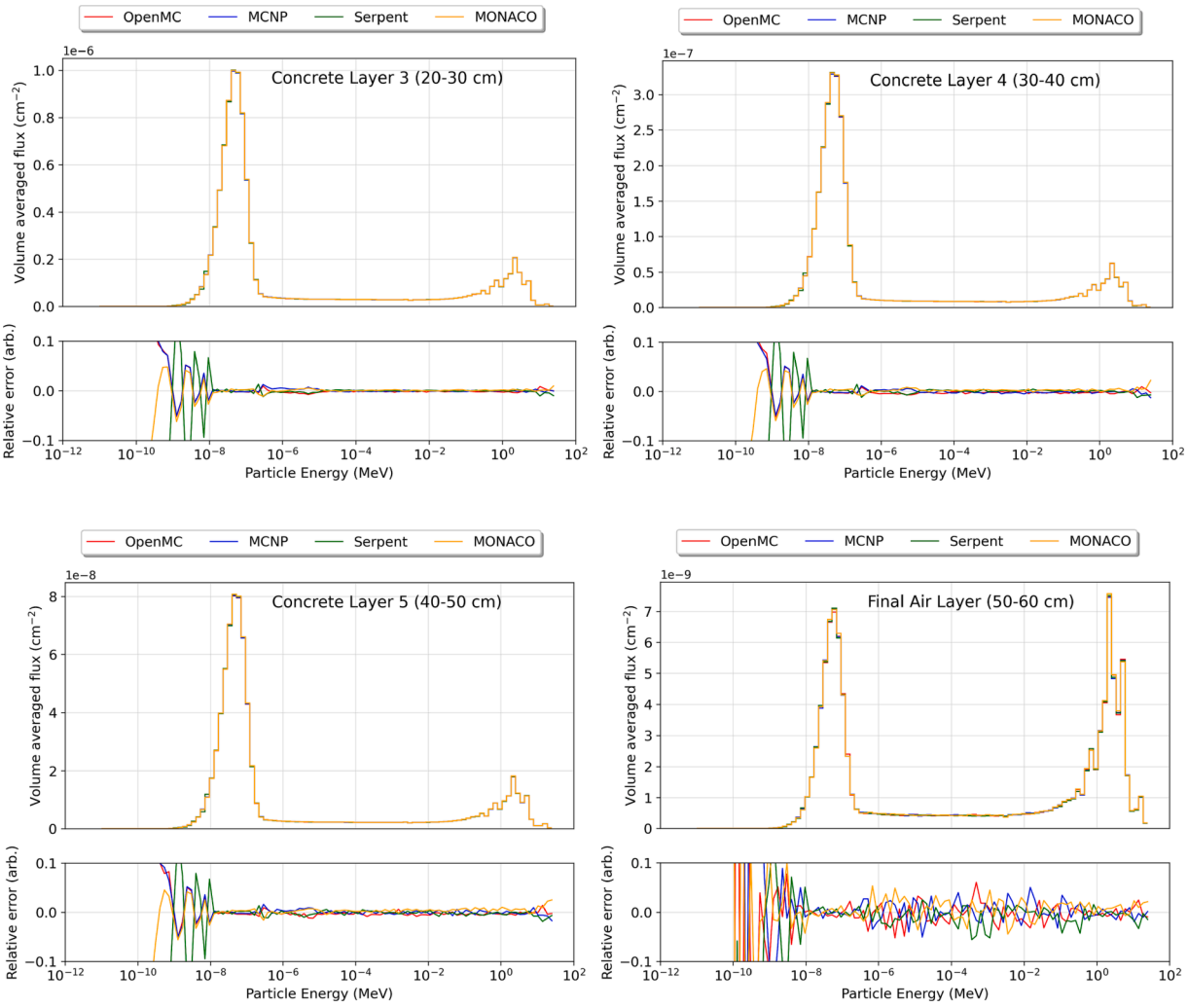

Fig. 8. Volume averaged flux in concrete layers 3–5 and air in relation to particle energy. The upper plots show the volume averaged neutron flux spectra from various codes while the lower plots describe the relative error from the mean of all codes.

Fig. 6.

Differences in flux calculations of the five studied codes are negligible. The relative error in the average flux of all codes does not exceed 0.01. The volume averaged flux decreases exponentially in subsequent layers as expected.

3.2. *Validation of neutron flux in standard concrete from SNF source*

Agreement of codes in photon transport is sufficient for evaluating most radioactive waste packaging materials. However, the evaluation of materials purposed for spent fuel disposal requires the modeling of neutron transport as well. For this purpose, the basic concrete geometry was combined with a SNF neutron spectrum to simulate the attenuation of neutrons in concrete. For this cross-comparison, the EGSnrc code was not included (no neutron transport capability). The neutron volumetric flux in all material layers is presented in Figs. 7 and 8. The SNF neutron flux demonstrated similar statistical errors as the LLW source simulation in the previous section.

The neutron flux spectra demonstrate two regions of interest. The lower-energy region with a local peak can be attributed to the thermalization of source neutrons while the higher-energy region of fast neutrons comes from neutrons scattered by the shielding concrete nuclei. Between the thermal and fast neutrons lies the epithermal plateau, mostly created by the thermalization process of fast neutrons going through elastic scattering, but also partly attributable to the original source term.

Similarly to the LLW photon modeling, the codes demonstrate a good agreement for the majority of the energy bins. Significant differences between codes appear only for low-energy slow neutrons with energies below 0.01 eV. Large disagreement in the slow neutron energy flux will not be a problem when evaluating the radiation shielding properties of innovative concretes. For this reason, the relative error (except the first layer), is shown in higher detail to demonstrate the values for the majority of the energy bins. The relative error from the mean value did not exceed 0.05 for higher energy neutrons. The rest of the layers demonstrated similar spectra and relative errors from mean outputs. The only exception to this rule was the final air layer, where the codes started to deviate more from mean behavior, but no biases were detected. This could partly be explained by the order of magnitude lower flux in the final air layer compared to the concrete preceding it.

The energy spectrum gives a good overview of particle transport code behavior, but it is just as important to characterize the total neutron flux in each layer. The total flux is demonstrated in Fig. 9.

Any deviations between code outputs are minimal when characterizing the total neutron flux of different layers. The relative error increases with each subsequent volume. Out of the transport codes, MONACO had the tendency to estimate slightly higher fluxes than the rest of the codes in the final layers, where the total source flux had been reduced by several orders of magnitude, but all the codes deviated by less than 0.01.

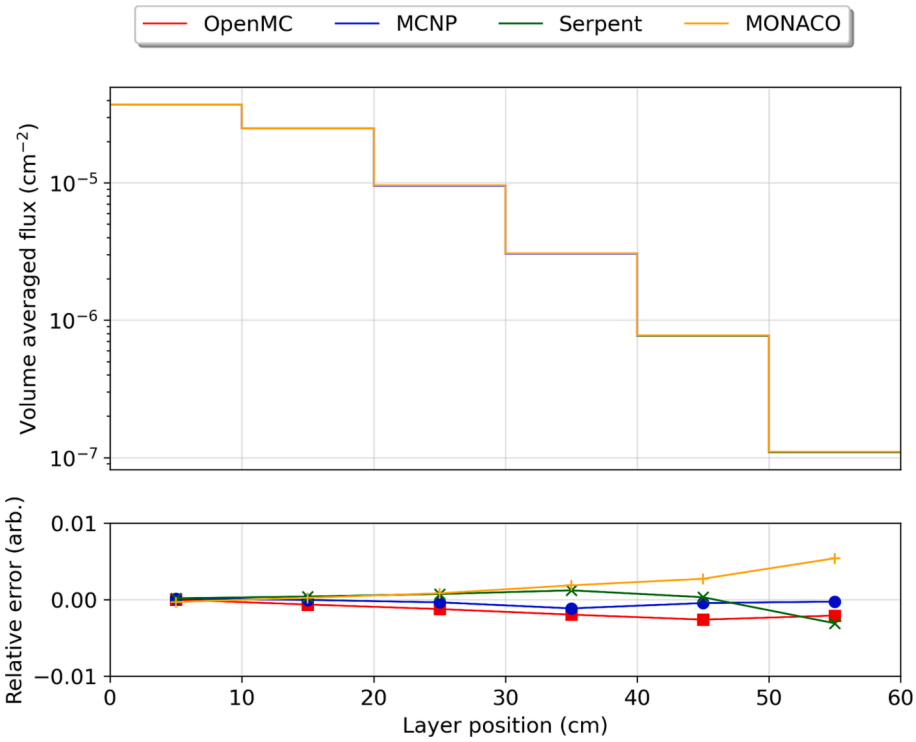

Fig. 9. The upper plot displays the comparison of volume averaged neutron flux spectra from various codes. Flux is presented in relation to tallied layer position. The lower plot describes the relative error (deviation from the mean of all results). Fig. 10: Volume averaged flux in concrete layers 1 and 2 in relation to particle energy. The upper plots show the volume averaged neutron flux spectra from various codes while the lower plots describe the relative error from the mean of all codes.

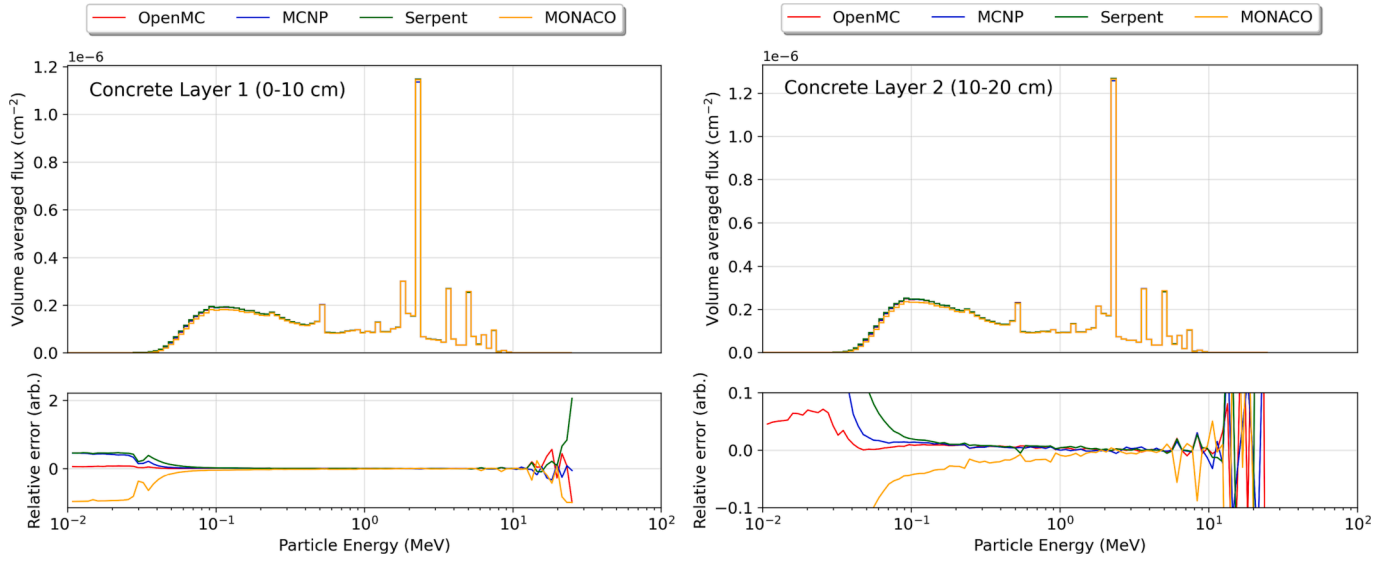

Fig. 10. Volume averaged flux in concrete layers 1 and 2 in relation to particle energy. The upper plots show the volume averaged neutron flux spectra from various codes while the lower plots describe the relative error from the mean of all codes.

3.3. Validation of activation photon flux in standard concrete from SNF source

Shielding of neutron flux can be divided into two categories, attenuation of neutrons and management of resultant gamma-photons created by the activation of concrete. Most Monte Carlo codes can transport activation photons simultaneously to neutrons. This functionality is present in OpenMC, MCNP, Serpent and MONACO. The activation flux was calculated in all concrete layers. The results are displayed in Figs. 10 and 11. The activation photon flux simulations were accompanied by similar statistical errors as previously presented cases (on average below 1 %, except for very low energies, where the flux was near zero).

The overall spectra are like those from the LLW source. They feature a broad Compton scattering peak as well as several smaller characteristic peaks, which have been emitted by the activated nuclei in concrete. The characteristic peak with the highest intensity corresponds to the H-1 neutron capture event during which 2.2 MeV gamma-photon is emitted with a 100 % probability.

The codes demonstrate good agreement from about 100 keV to

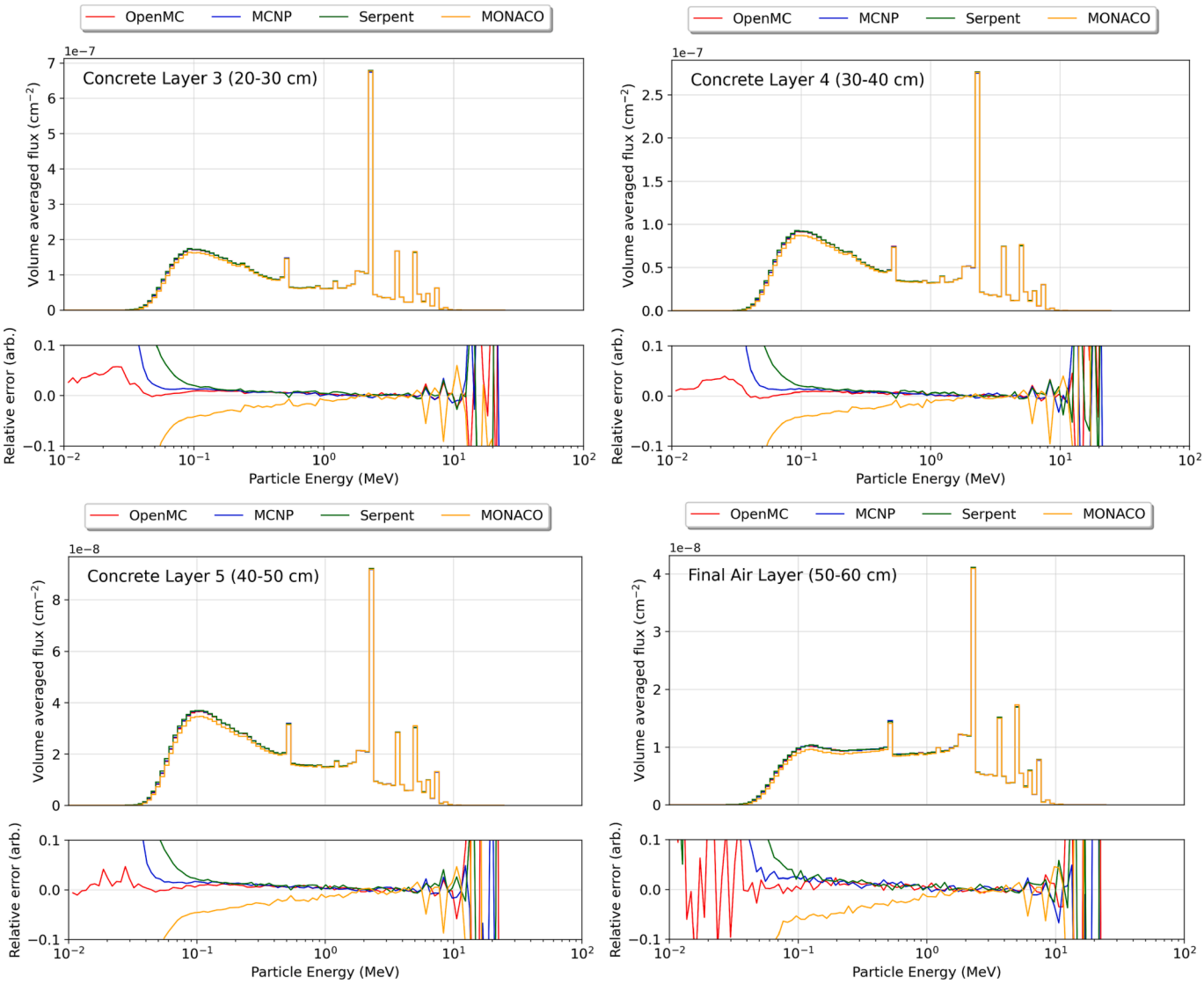

Fig. 11. Volume averaged flux in concrete layers 3–5 and air in relation to particle energy. The upper plots show the volume averaged activation photon flux spectra from various codes while the lower plots describe the relative error from the mean of all codes.

around 10 MeV. Below 100 keV, significant differences in fluxes start to appear, with MONACO showing the biggest deviations from the arithmetic mean of all code outputs. MCNP and Serpent predict quite equivalent results, while OpenMC's estimation follows the mean closely. Since the most important region from the viewpoint of radiation protection is above 100 keV but below 10 MeV, where the results show good agreement, all codes seem well applicable for activation calculations. Comparable results were observed for all volumes of the geometry, where the relative error in the region of interest did not increase above 0.1.

The total photon flux in all layers is described in Fig. 12. The total photon flux illustrates a small bias in the MONACO code when compared to other flux calculations. However, it should be noted that this bias is insignificant enough to make MONACO well-suitable for similar evaluations.

3.4. Photon shielding capability of innovative concrete

After confirming that all radiation transport codes provide results in good agreement, the same model was used to assess the radiation shielding properties of innovative oil shale, basalt fiber and basalt-boron fiber concretes. The radiation shielding properties were compared to each other by calculating the volume averaged energy flux in the last air layer. Similarly to the NIST concrete, all the codes demonstrated excellent agreement with each other.

For the majority of LLW photon energy flux estimations, the difference in energy flux was less than 5 % and less than 1 % for the total flux. However, an outlier was observed in the estimation of neutron flux of OL-E concrete as MONACO predicted approximately 2.5 % lower total flux than the other code. The statistical uncertainty in the photon simulations remained on average below 5 % (95 % confidence interval) for the energy flux and below 1 % for the total flux. The uncertainty increases above the presented level only for the marginal flux energy regions.

The results for the LLW source are displayed in Fig. 13. The concrete's capability to attenuate radiation was heavily correlated with the concrete's density. The highest density concretes were OL-E and OL-A (2.339 and 2.333 respectively), which demonstrated the lowest flux values behind the concrete. The minor trace elements had a marginal influence on the photon flux, indicating that the addition of OSA influences the final concrete's radiation shielding properties similarly to already characterized fly ash.

It should be noted that the shape of the energy spectra was not influenced by the chemical composition of the innovative concrete. The

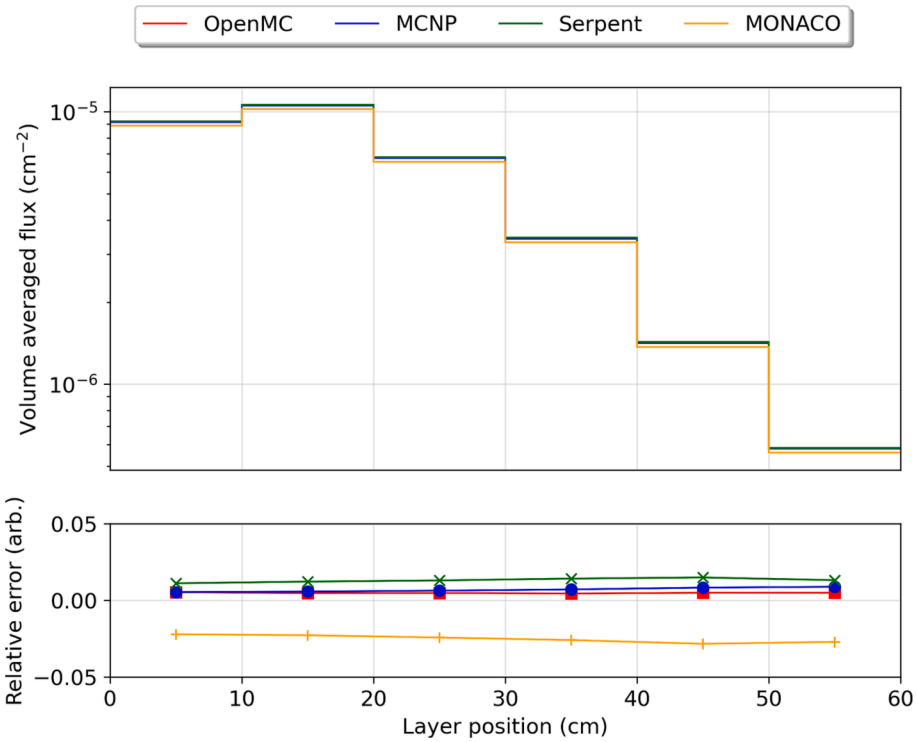

Fig. 12. The upper plot displays the comparison of volume averaged activation photon flux spectra from various codes. Flux is presented in relation to tallied layer position. The lower plot describes the relative error (deviation from the mean of all results).

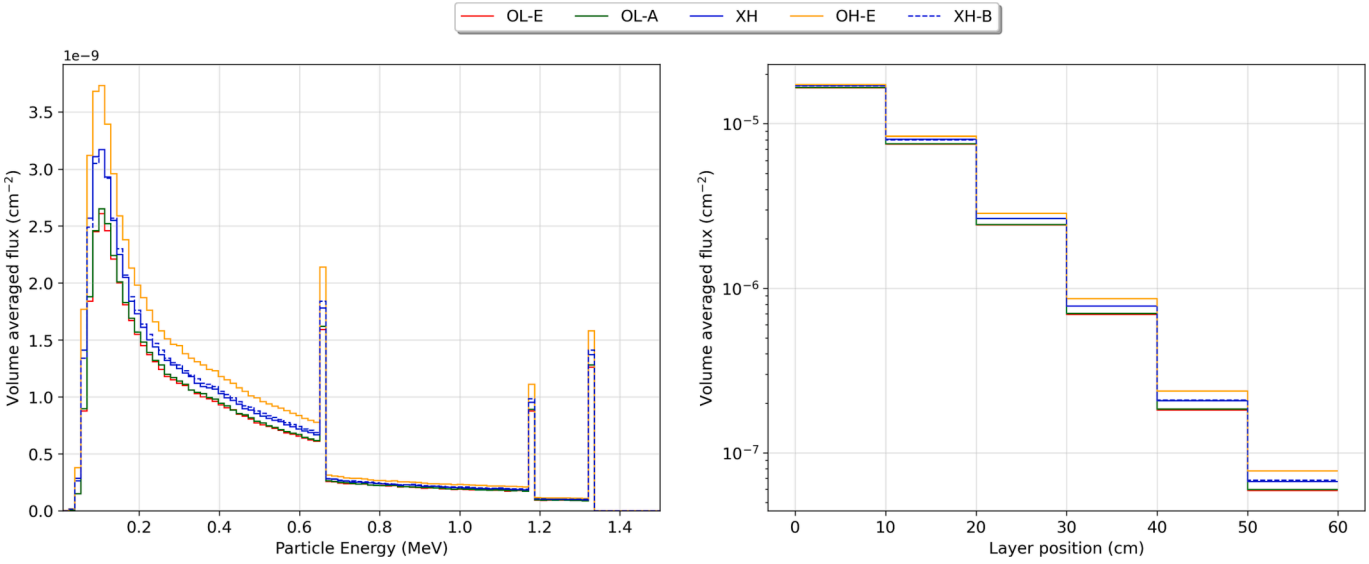

Fig. 13. The left plot describes the LLW source photon flux distributed in energy for investigated concrete recipes, while the right plot demonstrates the total flux distribution in scored layers.

highest intensity emissions behind the innovative concrete types were attributable to Compton scattering taking place inside the concrete, with average energies around 100 keV. The chemical composition was observed to have a weak effect on the total volume averaged flux in different concrete layers. The replacement of basalt-fibers with BBF had a small but negative influence on the attenuation capability with a difference of 2 % in total flux.

3.5. Neutron and activation photon shielding capability of innovative concrete

When the LLW source was replaced with the SNF source, larger differences in the volume average flux were observed. The volume averaged neutron flux distribution in energy is illustrated in Fig. 14. Similarly to the LLW source, the statistical errors for the neutron flux were small. On average below 5 % for the energy flux and 1 % for the total flux. Higher than 5 % was reported only for energies with near zero flux. The activation photon fluxes were accompanied by similar levels of uncertainty as well. Both types of estimations displayed equivalent

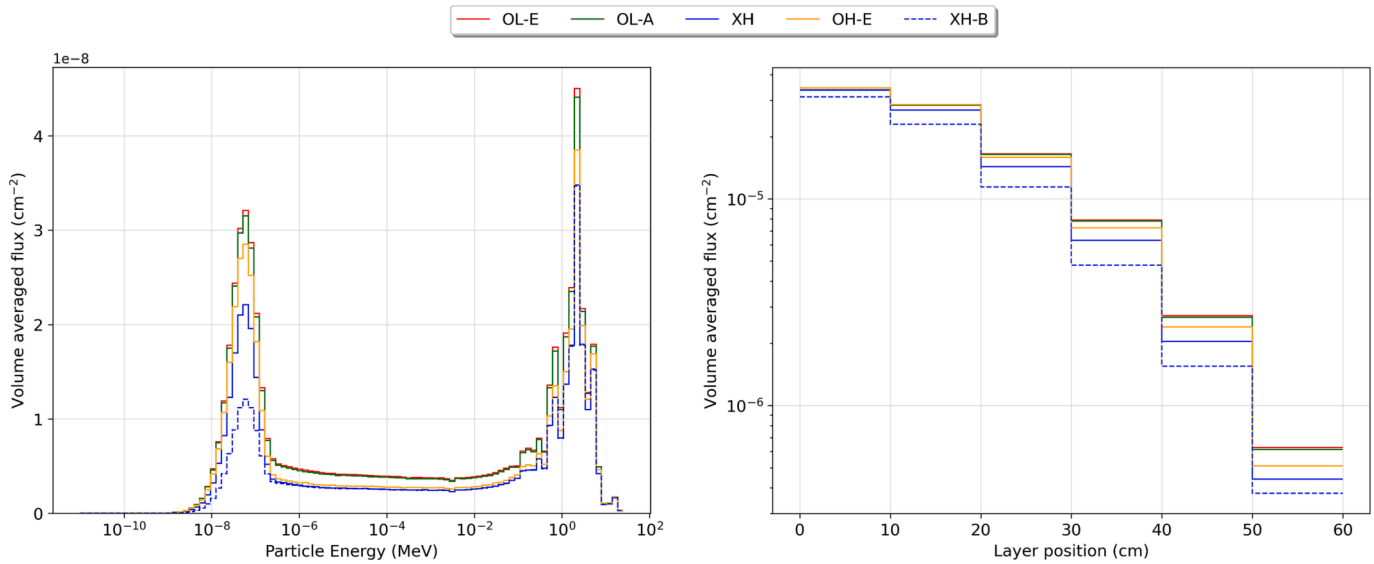

Fig. 14. The left plot describes the neutron flux distributed in energy for investigated concrete recipes, while the right plot demonstrates the total flux distribution in scored layers.

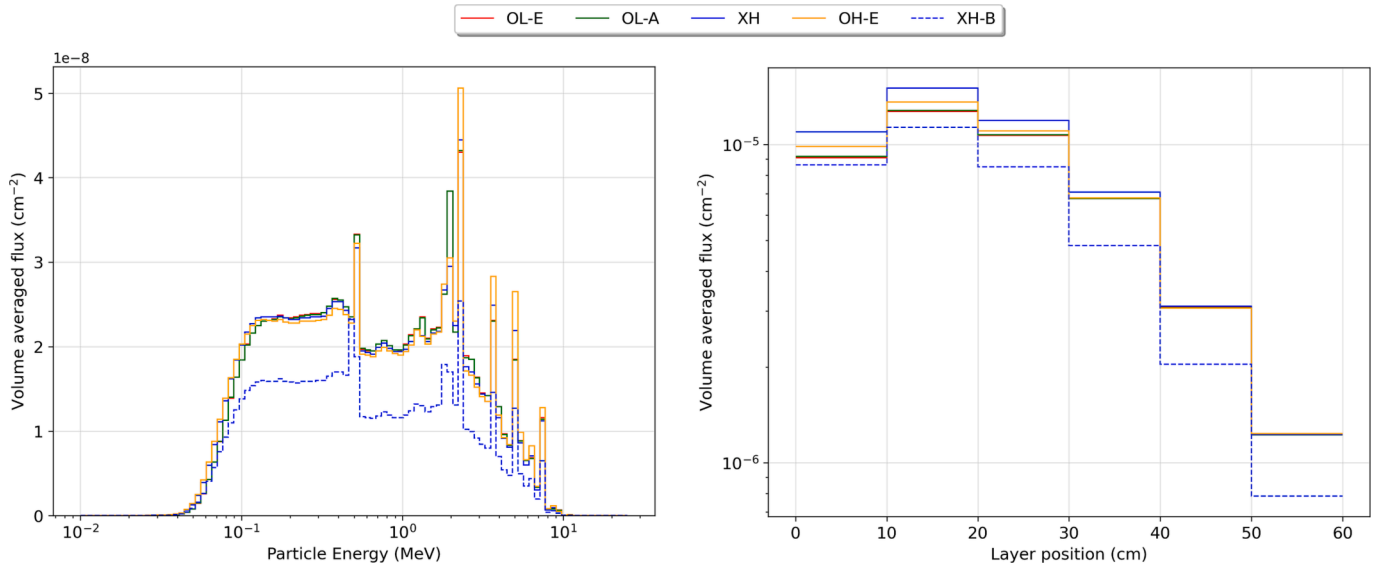

Fig. 15. The left plot describes the neutron activation photon flux distributed in energy for investigated concrete recipes, while the right plot demonstrates the total flux distribution in scored layers.

agreements between codes as the cross-comparison of NIST concrete.

Out of all the concretes, XH-B demonstrated the lowest neutron flux values in the last air layer. The comparison between XH and XH-B concrete demonstrated that the use of BBF significantly decreases the thermal energy neutron flux (absorption by added boron isotopes) but showed no large-scale changes in the epithermal and fast energy region. In summary, the replacement of basalt fibers with BBF in the XH concrete induced large changes in the thermalized neutron flux spectra.

The OSA concretes showed similar properties to fly ash concrete in the attenuation of neutrons. The addition of OSA had a marginal negative impact on concrete's ability to attenuate neutrons. The low hydration oil shale concretes OL-E and OL-A were characterized by the highest neutron flux behind the concrete. Concrete's ability to reduce neutron flux was heavily correlated with the water content. Increasing the water content of OSA concretes (OH-E) notably improved the moderation capability, leading to lower flux values.

The analysis of activated photon flux (Fig. 15) showed on average an inverse correlation between neutron flux and activation photon flux values for the initial concrete layers. The higher neutron attenuation capability of concrete resulted in a stronger activation flux. The XH concrete was responsible for the highest activated photon flux in the initial concrete layer, but the flux decayed over the distance. It is likely that as neutrons interact more with the concrete more activated isotopes will be created, resulting in a higher activation photon flux.

The replacement of basalt fibers with BBF in the XH concrete induced significant deviations from this trend. Unlike other concretes, where a decrease in the neutron flux induced an increase in the activation photon flux, the basalt-boron concrete demonstrated an overall lower photon flux throughout all the scored layers. When other concretes converged to roughly the same total activation photon flux value, the influence of BBF did not become insignificant, with the total flux difference in the final air layer being around 55 %.

Similarly to the standard NIST concrete, the highest activation photon peak was observed to be due to the neutron capture by H-1 (most

prominent in concretes with high water content). The second highest peak, and the peak that varied the most across the different concrete recipes was produced by the neutron activation of Ca-40. In the relaxation process Ca-40 emits a 1.943 MeV gamma-ray. OL-E and OL-A concretes, where the Ca content was almost twice as high as other concretes, demonstrated correspondingly almost twice as high flux values for that energy bin.

Overall, the results indicate that the addition of OSA can have a minor effect on the activation of photon emissions by decreasing the number of thermal neutrons available for capture. However, it should be noted that there are some isotopes such as Ca-40 whose concentration can be increased by the usage of OSA or comparable additives. The presence of these isotopes in higher concentrations can be correlated with an increase in the emission of high-energy gamma-photons.

4. Conclusions

The impact of using innovative additives in radioactive waste packaging was analyzed. The main goal of the study was to investigate whether five Monte Carlo codes (MCNP, SERPENT, SCALE, OpenMC, and EGSnrc) can be reliably used to characterize the interactions between radiation and concrete additives such as oil shale ash and basalt-boron fibers. For this purpose, simple model geometry was created and combined with emissions from realistic low-level and high-level radioactive wastes. 5 different concrete recipes were prepared and characterized using radiation shielding calculations.

The investigations using NIST concrete showed excellent agreement between all the codes. The volume averaged energy spectra deviated by less than 5 % for the majority of energy bins for both gamma and neutron radiation. Larger deviations were only observed in regions of low flux or energy. Similar results were observed for the activation photon flux in concrete as well. It should be noted that SCALE demonstrated slightly larger deviations in activation photon calculations compared to the rest of the codes.

The addition of oil shale ash had a negligible impact on the concrete's ability to shield radiation from low-level radioactive waste. For spent nuclear fuel, the additive had a marginal but negative impact on neutron shielding properties and a minor effect on the activation photon emissions by decreasing the number of thermal neutrons available for capture. The analysis showed that oil shale ash behaves similarly to fly ash characterized in the literature.

The addition of basalt-boron fibers had a marginal but negative effect on the photon shielding properties but increased the concretes' ability to shield neutrons significantly. In a similar vein, the activation photon flux was noticeably lower as well. These investigations demonstrated that all five Monte Carlo codes can reliably be used to characterize interactions between radiation from radioactive waste and potential concrete additives. The characterized additives show great promise in their purpose. The addition of oil shale ash to reduce the mobility of radionuclides can be done without significant degradation of radiation shielding properties and basalt-boron fibers have demonstrated excellent capability to increase the concretes' neutron shielding properties.

Funding

This work was carried out within the "Innovation in concrete design for hazardous waste management applications" (ICONDE) project, EEA-RESEARCH-165, financially supported by the European Economic Area (EEA) Grants of Iceland, Liechtenstein, and Norway.

CRediT authorship contribution statement

Hando Tohver: Methodology, Software, Validation, Formal analysis, Writing – original draft, Visualization. **Andrius Slavickas:** Methodology, Software, Validation, Writing – review & editing. **Maryna Holiuk:** Methodology, Software, Validation, Writing – review & editing. **Andrejs Krasņikovs:** Resources, Writing – review & editing. **Riho Mõtlep:** Resources, Writing – review & editing. **Iveta Nováková:** Writing – review & editing. **Mindaugas Vaišnoras:** Writing – review & editing, Supervision. **Volodymyr Gulik:** Conceptualization, Methodology, Supervision.

Declaration of competing interest

The authors declare that they have no known competing financial interests or personal relationships that could have appeared to influence the work reported in this paper.

Data availability

Data will be made available on request.

References

Abdullah, M.A., Rashid, R.S., Amran, M., Hejazii, F., Azreen, N.M., Fediuk, R., Idris, M.I., 2022. Recent trends in advanced radiation shielding concrete for construction of facilities: materials and properties. Polymers. https://doi.org/10.3390/polym14142830.

Ageing management of concrete structures in Nuclear Power Plants. (2016). Vienna: IAEA Nuclear Energy Series No. NP-T-3.5, IAEA, pp. 353.

Bé, M.M., Chisté, V., Dulieu, C., Mougeot, X., Chechev, V., Kondev, F.G., Wang, B., 2013. Table of Radionuclides, Volume 7. Bureau International des Poids et Mesures, Sèvres.

Berger, M.J., Coursey, J.S., Zucker, M.A., Chang, J., 2017. NIST Standard Reference Database 124. NIST, Physical Measurement Laboratory, Gaithersburg, Maryland.

Catenacci, M.J., Luckarift, H.R., Friedman, R.J., Male, A., Owens, J.R., 2021. Effect of fly ash composition and component quantities on the gamma radiation shielding properties of geopolymer. Prog. Nucl. Energy. https://doi.org/10.1016/j.pnucene.2021.103889.

Chen, Q.Y., Tyrer, M., Hills, C.D., Yang, X.M., Carey, P., 2009. Immobilisation of heavy metal in cement-based solidification/stabilisation: a review. Waste Manag. 390–403. https://doi.org/10.1016/j.wasman.2008.01.019.

Han, M.C., Pia, M.G., Saracco, P., Basaglia, T., 2018. First Assessment of ENDF/B-VIII and EPICS Atomic Data Libraries. IEEE Trans. Nucl. Sci. 2268–2278. https://doi.org/10.1109/TNS.2018.2849328.

Kharita, M.H., Yousef, S.A., 2011. Review on the addition of boron compounds to radiation shielding concrete. Prog. Nucl. Energy 207–211. https://doi.org/10.1016/j.pnucene.2010.09.012.

Koťátková, J., Zatloukal, J., Reiterman, P., Kolář, K., 2017. Concrete and cement composites used for radioactive waste deposition. J. Environ. Radioact. 147–155. https://doi.org/10.1016/j.jenvrad.2017.08.012.

Leben, K., Mõtlep, R., Paaver, P., Konist, A., Pihu, T., Päärn, P., Kirsimäe, K., 2019. Long-term mineral transformation of Ca-rich oil shale ash waste. Sci. Total Environ. 1404–1415. https://doi.org/10.1016/j.scitotenv.2018.12.326.

Leppänen, J., Pusa, M., Viitanen, T., Valtavirta, V., Kaltiaisenaho, T., 2013. The Serpent Monte Carlo code: Status, development and applications in 2013. Ann. Nucl. Energy 142–150. https://doi.org/10.1016/j.anucene.2014.08.024.

Li, J., Chen, L., Wang, J., 2021. Solidification of radioactive wastes by cement-based materials. Prog. Nucl. Energy. https://doi.org/10.1016/j.pnucene.2021.103957.

Loo, L., Maaten, B., Konist, A., Siirde, A., Neshumayev, D.P., 2017. Carbon dioxide emission factors for oxy-fuel CFBC and aqueous carbonation of the Ca-rich oil shale ash. Energy Procedia 144–149. https://doi.org/10.1016/j.egypro.2017.09.034.

Mallants, D., Ochs, M., Wang, L., 2016. Radionuclide and Metal Sorption on Cement and Concrete. Springer, Cham.

Meija, J., Coplen, T.B., Berglund, M., Brand, W.A., Bièvre, P.D., Holden, N.E., Prohaska, T., 2016. Isotopic compositions of the elements 2013 (IUPAC Technical Report). Pure Appl. Chem. https://doi.org/10.1515/pac-2015-0503.

Öztürk, B.C., Kızıltepe, C.Ç., Ozden, B., Güler, E., Aydın, S., 2020. Gamma and neutron attenuation properties of alkali-activated cement mortars. Radiat. Phys. Chem. https://doi.org/10.1016/j.radphyschem.2019.108478.

Piotrowski, P., 2021. Neutron shielding evaluation of concretes and mortars: a review. Constr. Build. Mater. https://doi.org/10.1016/j.conbuildmat.2020.122238.

Romanenko, I., Holiuk, M., Kutsyn, P., Kutsyna, I., Odynokin, H., Nosovskyi, A., Gulik, V., 2019. New composite material based on heavy concrete reinforced by basalt-boron fiber for radioactive waste management. EPJ Nuclear Sciences & Technologies. https://doi.org/10.1051/epjn/2019050.

Romano, P.K., Horelik, N.E., Herman, B.R., Nelson, A.G., Forget, B., Smith, K., 2015. OpenMC: a State-of-the-art monte carlo code for research and development. Ann. Nucl. Energy 82, 90–97.

Singh, S., Singh, K., Singh, G., 2014. Effect of flyash addition on mechanical and gamma radiation shielding properties of concrete. Journal of Energy. https://doi.org/10.1155/2014/486093.

Werner, C. J. (2017). *MCNP Users Manual - Code Version 6.2 (report LA-UR-17-29981).* Los Alamos, New Mexico: Los Alamos National Laboratory.

Wiarda, D., Dunn, M.E., Greene, N.M., Celik, C., Petrie, L.M., 2016. AMPX-6: A Modular Code System for Processing ENDF/B (ORNL/TM-2016/43). Oak Ridge National Laboratory, Oak Ridge, Tennessee.

Wieselquist, W. A., Lefebvre, R. A., & Jessee, M. A. (2020). *SCALE Code System, ORNL/TM-2005/39, Version 6.2.4 (CCC-834)*. Oak Ridge, Tennessee: Oak Ridge National Laboratory.

Zorla, E., Ipbüker, C., Biland, A., Kiisk, M., Kovaljov, S., Tkaczyk, A.H., Gulik, V., 2017. Radiation shielding properties of high performance concrete reinforced with basalt fibers infused with natural and enriched boron. Nucl. Eng. Des. 306–318. https://doi.org/10.1016/j.nucengdes.2016.12.029.